buildings

MDPI

Article

Rotational Stiffness Investigation and Parametric Analysis of a Novel Assembled Joint in Lattice Shells

Jianshe Xu [1], Yazhi Zhu [2,*], Jin Wu [1], Jin Lu [1,3], Qian Zhang [1,4] and Wei Wang [2]

[1] Department of Civil Engineering, University of Shanghai for Science and Technology, Shanghai 200093, China
[2] Department of Structural Engineering, Tongji University, Shanghai 200092, China
[3] Hangzhou Yuexiu Real Estate Development Co., Ltd., Hangzhou 311305, China
[4] Shanghai Pudong New Area Construction (Group) Co., Ltd., Shanghai 200120, China
* Correspondence: yzzhu@tongji.edu.cn

Abstract: Although there are currently many types of lattice shell joints with different characteristics, assessing the flexural capacity of lattice shell joints is always a great challenge. In this paper, a fan-shaped assembled joint and a welded joint for comparison were subjected to bending tests to investigate the flexural behavior and rotational stiffness of the assembled joint. The strain distribution, load–displacement curve, moment–rotation curve, and damage modes of key parts were analyzed to determine the vulnerable parts of the joints. Our test results show that, with an initial rotational stiffness of about one third of that of the welded joint, the assembled joint specimen exhibits the obvious characteristics of a semi-rigid joint. The finite element analysis results were in good agreement with the experimental results. The results of our parametric analysis show that the rotational stiffness and ultimate moment of the assembled joint increase with increases in the spacing of the bolts and the number of bolts. The performance of the high-strength bolts had a significant influence on the flexural stiffness of the assembled joints. The spacing of the bolts and the number of bolts for the assembled joint are suggested to be greater than the height of the member section and more than three, respectively. The proposed theoretical formula can approximately simulate the initial rotational stiffness of the joint. More in-depth investigations are required in the future for assessing the mechanical behavior of FSA joints subjected to combined bending–compression loads.

Keywords: curved lattice shells; assembled joints; rotational stiffness; bending tests

check for updates

Citation: Xu, J.; Zhu, Y.; Wu, J.; Lu, J.; Zhang, Q.; Wang, W. Rotational Stiffness Investigation and Parametric Analysis of a Novel Assembled Joint in Lattice Shells. *Buildings* **2024**, *14*, 261. https://doi.org/10.3390/buildings14010261

Academic Editor: Hassan Karampour

Received: 1 December 2023
Revised: 10 January 2024
Accepted: 16 January 2024
Published: 17 January 2024

Copyright: © 2024 by the authors. Licensee MDPI, Basel, Switzerland. This article is an open access article distributed under the terms and conditions of the Creative Commons Attribution (CC BY) license (https://creativecommons.org/licenses/by/4.0/).

1. Introduction

Owing to their advantages of high stiffness, good stability, reasonable force distribution, economic favorability, and environmental friendliness [1–3], reticulated lattice shell structures have been widely used in practice. The traditional joint type of a single-layer reticulated shell structure is a welded joint [4,5]. In recent years, to reduce on-site welding workloads, various new types of lattice shell joints have emerged in large numbers. Among these joints, bolted spherical joints [5–9] and socket joints [10] connect a member with only one bolt, so their overall flexural performance is relatively weak. A gear–bolt joint [11,12] places a gear–bolt at the middle of the connecting plate to bear bending moments. A bolt–column–plate joint [13] has enough out-of-plane rotational stiffness, but is weak under in-plane bending. Ball–cylinder joints [14], pre-embedded bolt joints [15,16], semi-rigid pin joints [17,18], dovetail joints [19–22], assembled hub joints [23–25], and SLO joints [26] require high installation accuracy since they connect shell members by threading the bolts into holes with internal threads instead of conventional bolt holes with installation clearance. Prestressed high-strength bolt joints [27] and semi-rigid pin joints [17,18] have complex joint details, similar to precision mechanical parts. Joints with overlapping tube sections [28,29] have a bit of difficulty in installation. Double-ring joints [30,31] connect members by two ring plates. A concrete-filled tubular joint [32,33] has a concrete pouring process. The joint in reference [34] is applicative only in specific architectural space frames.

Temcor or similar gusset joints [35–38] are generally used in aluminum alloy structures with I-shaped sections. Plate-type joints [39] are suitable in shells with plate members. Miao et al. [40] assessed the flexural stiffness of cylindrical shells by introducing a six-bar tetrahedral unit. A combined nested bolted joint [41] connects each shell member with a protruding sleeve and several one-side bolts.

Previous studies indicate that the joints in lattice shells face difficulties in terms of flexural performance (load-carrying capacity and stiffness). To address the issue of flexural capacity, a novel assembled joint for curved lattice shells (i.e., fan-shaped assembled joint) is proposed in this study. As shown in Figure 1, the joint can comprises several fan-shaped components based on the number of members. All of the components are connected to the rib plates using high-strength bolts inside the joint. The fabrication and welding of the members and joints are all conducted in the factory, so field welding is no longer needed. It is clear that each component of the joint is connected to a corresponding member in the factory fabrication stage instead of in the erection stage, as is the case with other types of joints.

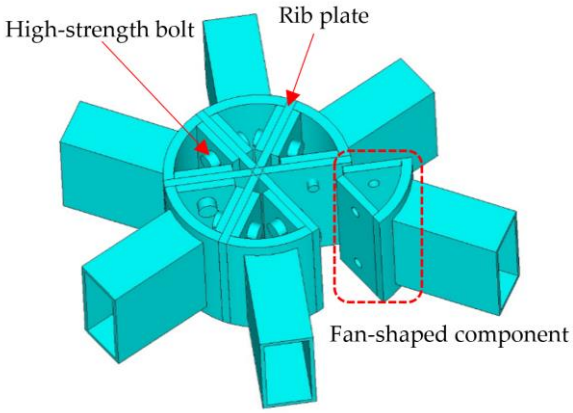


Figure 1. Schematic illustration of the fan-shaped assembled joint.

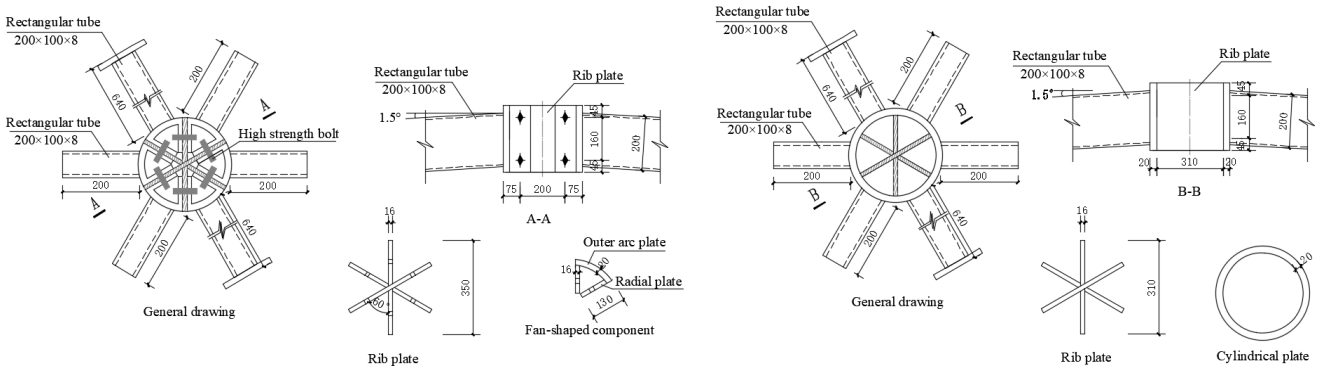
The fan-shaped assembled joint (hereinafter referred to as the FSA joint) has significant differences from other types of lattice shell joints in terms of constructional details, load transfer mechanisms, etc. In this study, to explore the flexural behavior and rotational stiffness of the FSA joint, bending tests were conducted on specimens both of the FSA joint and the welded joint. The latter can be considered to possess large rigidity and was used for comparative purposes. The mechanical performances of the joints were compared by their bending moment–rotation curve characteristics, rotational stiffness, and failure modes. Subsequently, the rotational stiffness of the assembled joint was studied by conducting both theoretical and numerical analyses.

2. Experimental Program

2.1. Specimens

The two specimens are named J-A and J-W, respectively. The former denotes the FSA joint, and the latter denotes the welded joint. Both joints were subjected to bending tests under moments caused by transverse load. In specimen J-A, each fan-shaped component was connected to a corresponding shell member with factory welds. The out-of-plane angles of all joints were set to 1.5°. Since the out-of-plane moment is usually much larger than the in-plane moment for single-layer lattice shell structures, an in-plane moment was not applied. Figure 2 shows detailed drawings of each specimen.

Q235B steel was used for all of the components of the specimens, including the members (rectangular steel tubes), ribs, and connecting plates. The high-strength bolts were all of grade 10.9. Material tests were conducted according to the standard tensile test method [42]. The mean value of the elastic modulus was 2.095×10^5 MPa. The yield strength (f_y), ultimate strength (f_u), and ultimate elongation rate (δ) are listed in Table 1, where t indicates the steel plate thickness.



(**a**) (**b**)

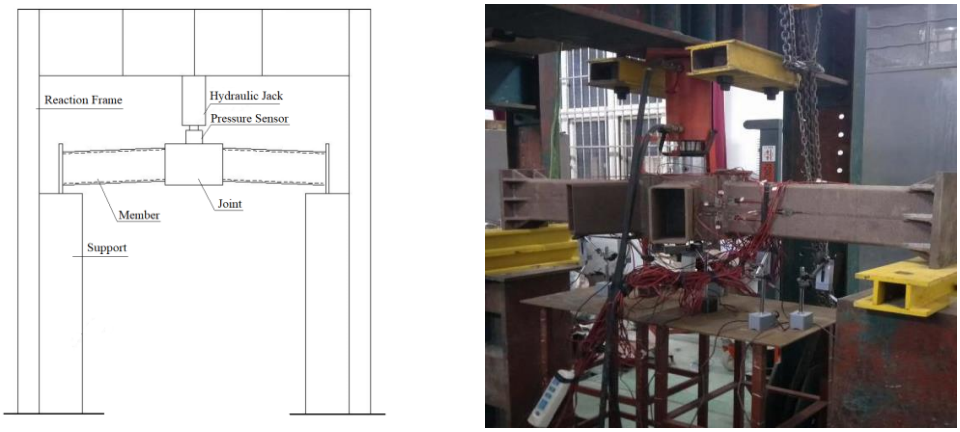
Figure 2. Detailed drawings of the specimens: (**a**) J-A (assembled joint); (**b**) J-W (welded joint). All dimensions in the drawings are in millimeters.

Table 1. Mechanical properties of the steels.

No.	t (mm)	f_y (MPa)	f_u (MPa)	δ (%)
1	8	269.52	404.29	31.23
2	16	274.90	433.08	31.67
3	20	270.31	411.62	30.00

2.2. Experimental Loading and Measurement Scheme

Figure 3 shows the experimental loading equipment, including a 50 t hydraulic jack. Static multi-stage loading was employed in both tests. The pre-loading level was 50 kN, and the maximum allowable loading value was set to 80% of the equipment tonnage, i.e., 400 kN. The specimen was located parallel to the ground, and thus, the hydraulic jack load was transverse. The load increments were set to 25 kN and 3 kN for load ranges of 0–180 kN and 180–400 kN, respectively. The specimen was considered to fail when either of the following conditions occurred: (1) excessive plastic deformation of the specimen occurred and the loading could not be continued; (2) obvious fracture occurred in any part of the specimen.



(**a**) (**b**)

Figure 3. Test setups: (**a**) schematic illustration; (**b**) specimen photo.

The layout of the measurement points is shown in Figures 4 and 5. A tension–compression sensor connected to the data acquisition system was placed under the hydraulic jack. The strain gauges were located in the area of large strain and at key parts of the joint based on the FEA results. The displacement gauges were arranged at the loading end, joint area, and support, respectively.

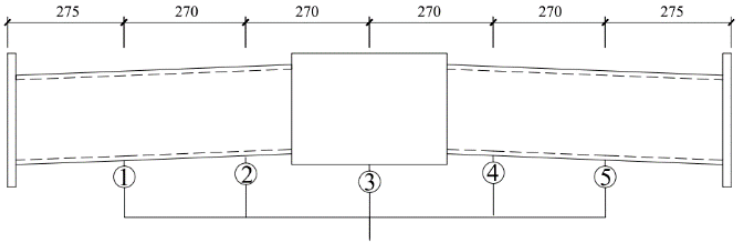


Figure 4. Layout of displacement gauges (numbers 1–5 represent gauge numbers).

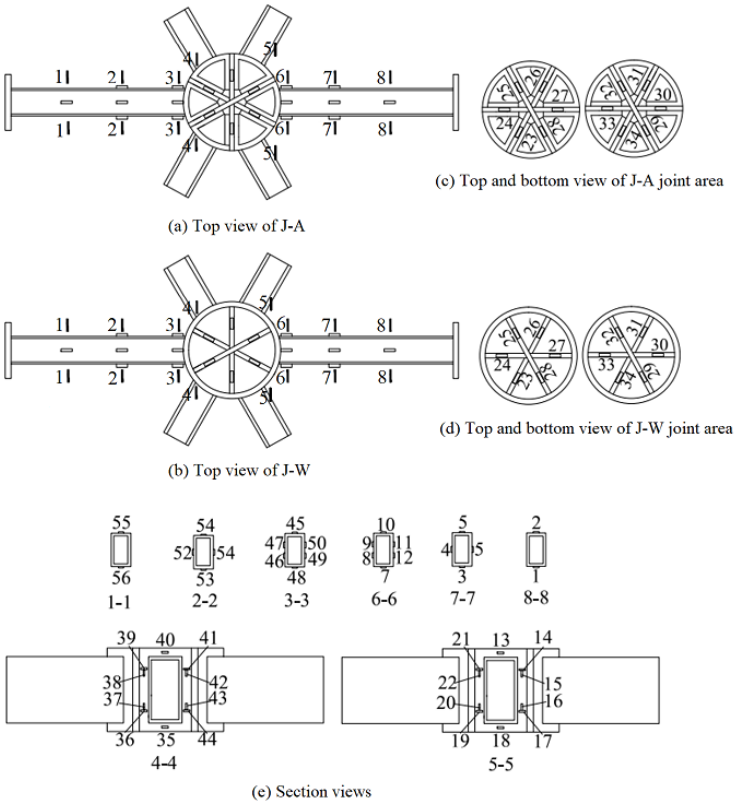


Figure 5. Layout of strain gauges (Numbers 1–8 with cutting lines represent section numbers, and numbers without cutting lines represent strain gauge numbers).

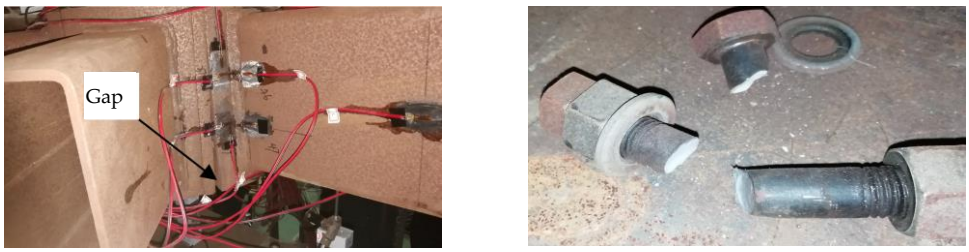
3. Experimental Results and Analysis

3.1. Experimental Phenomena

J-A: In the load range of 0 to 100 kN, the deformation at the specimen center increased gradually, and there was no marked change in the other parts. When the load increased to 175 kN, one strain gauge in the joint area yielded, and the strain values of the other strain gauges increased, but not dramatically. At this time, the gap between the rib plate and the fan-shaped component in the joint area was approximately 10 mm wide, and the joint moved downward noticeably. When the load was increased to 192 kN, shear failure of the two bolts at the lower end of the fan-shaped component occurred, and the joint deformation increased significantly. The loading was stopped upon failure of the specimen. The failure mode is shown in Figure 6.

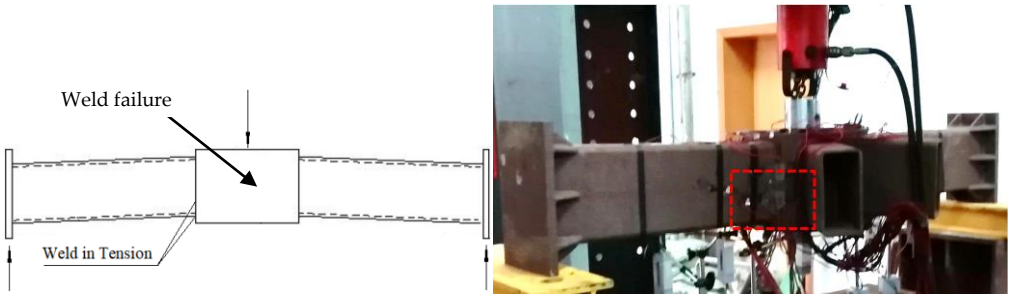
J-W: The specimen exhibited slight deformation under a load of 200 kN. When the load increased to 250 kN, the centroid of the specimen moved noticeably downward, and the strain gauges at the end of the member had basically yielded. When the load increased to 300 kN, the strain gauges on the joint plate yielded, while the member remained elastic, and the corresponding downward displacement at the specimen centroid was 12.7 mm. When the load reached 371 kN, the lower part of the weld connecting the member and the

joint failed due to the tension stress caused by the moment at the member end, and the loading was stopped owing to the failure of the specimen. The failure mode is shown in Figure 7.

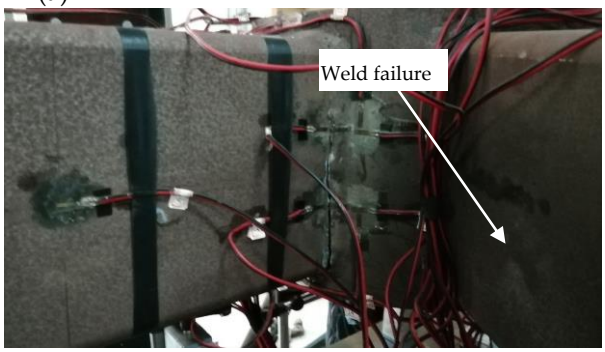


(**a**) (**b**)

Figure 6. Failure mode of specimen J-A. (**a**) Overall failure mode; (**b**) bolt failure.



(**a**) (**b**)



(**c**)

Figure 7. Failure position and mode of J-W. (**a**) Failure position schematic drawing; (**b**) failure position photo; (**c**) weld failure photo.

3.2. Moment–Rotation Curve

The rotational stiffness was calculated using the slope of the moment–angle curve. The bending moment–rotation curves for J-A and J-W are shown in Figure 8. It can be seen that J-W underwent three stages from loading to failure: (1) the elastic stage (0–163 kN·m), in which the moment–rotation curve is a straight line and the joint is basically in the elastic stage; (2) the elastic–plastic stage (163–293.4 kN·m), in which the moment–rotation relationship is no longer linear and the bending stiffness decreases continuously owing to the yielding of some strain gauges; and (3) the plastic failure stage (293.4–302.4 kN·m), in which the moment–rotation curve flattens gradually, most of the strain gauges in the joint area enter the plastic stage, and the plastic zone of the joint develops rapidly. Finally, the joint is damaged at the weld between the member and the joint.

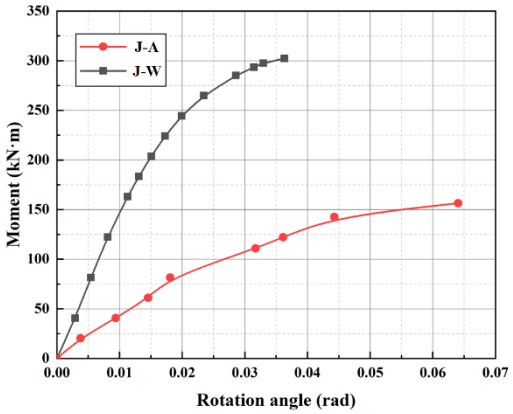


Figure 8. Moment–rotation curves of J-A and J-W.

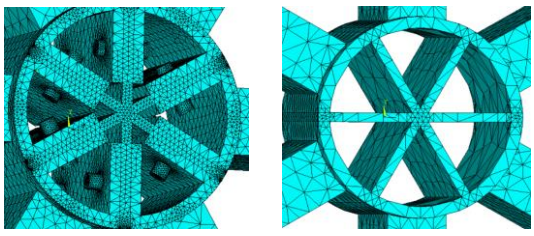
J-A also experienced three stages from loading to failure: (1) the elastic stage (0–81.5 kN·m), in which the bending stiffness is relatively large owing to the firm connection between the rib and the fan-shaped component; (2) the elastic–plastic stage (81.5–142.6 kN·m), in which the bending stiffness decreases markedly (the decrease reaches about half of the initial stiffness), and the rotation angle increases gradually owing to the deformation of the bolt hole wall; and (3) the plastic failure stage (143–156.5 kN·m), in which the rotational stiffness of the joint decreases dramatically, and the rotation of the joint increases sharply.

Figure 8 also indicates that the rotational stiffness and bending capacity of the assembled joint are both lower than those of the welded joint. The assembled joint exhibits the obvious characteristics of a semi-rigid joint. This is mainly due to the influence of bolt hole deformation. The initial rotational stiffness of the FSA joint is about one third of that of the welded joint.

4. Verification of FE Models

4.1. FE Models

FEA was conducted using ANSYS to simulate the evolution process of the stress characteristics of both joints. Each joint was modeled according to Figure 2. A 3D eight-node solid element with three degrees of freedom per node was used to mesh the models, which simulated the state of the specimen in a realistic manner. The joint area meshing of the FE models is shown in Figure 9, and the mechanical parameters were obtained from the experimental values for the materials. The contacts between the bolt head and inner surface of the radial plate of the fan-shaped component, outer surface of the radial plate and rib plate, nut and inner surface of the radial plate, bolt bar surface and radial plate, and bolt bar surface and rib plate were all defined as contact pairs.



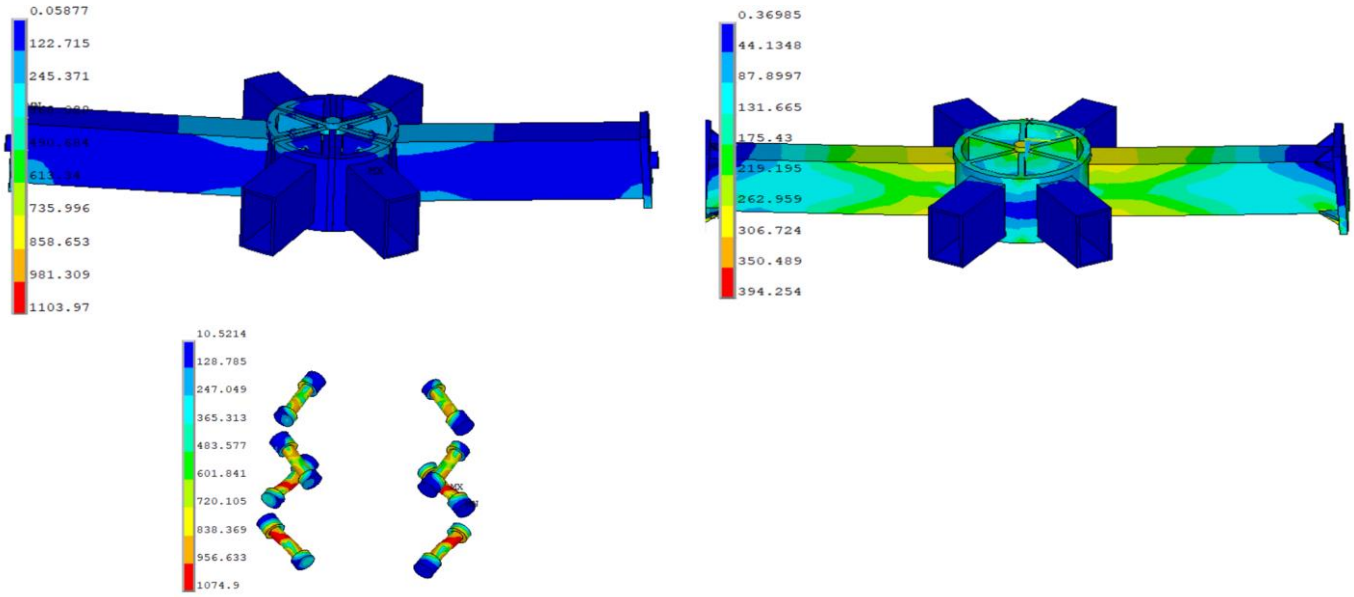
(**a**) (**b**)

Figure 9. Meshing of FE models: (**a**) assembled joint; (**b**) welded joint.

4.2. FEA Results

Figure 10 shows von Mises stress cloud diagrams for both specimens under the failure load. The maximum stress of J-W reaches 394 MPa, and the maximum stress occurs in the weld connecting the rectangular section member to the joint, indicating that the weld is

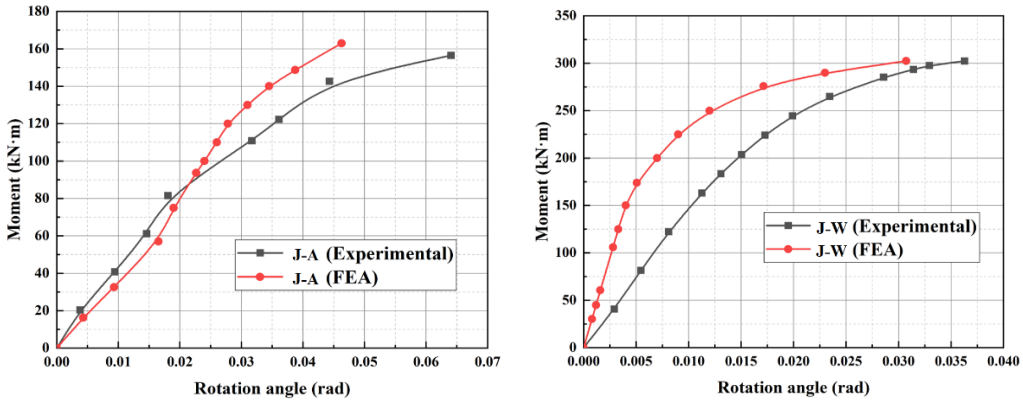
the weak point of the welded joint. This is consistent with the experimental results. For J-A, the maximum stress at the bolt is much larger than that at the weld. It also exceeds the yield stress (900 MPa), indicating that the bolt is the weak part of the assembled joint, which is also consistent with the experimental results.



(**a**) (**b**)

Figure 10. Contours of stress field: (**a**) J-A; (**b**) J-W.

Figure 11 shows a comparison between the FEA results and experimental bending moment–rotation curves. It can be seen that the rotation angle of J-W in the experiment is significantly larger than that of the FEA under the same bending moment owing to the difference between the ideal state of the FEA model and the existence of residual stresses in the welded specimen. For J-A, the rotation angle of the experiment is larger than that of the FEA under the same bending moment in the late loading period because the bolt starts to be stressed and there is a difference in the bilinear instantaneous model of the bolt between the FEA and experiment.



(**a**) (**b**)

Figure 11. Comparison of the experimental and FEA moment–rotation curves: (**a**) J-A; (**b**) J-W.

5. Parametric Analysis of the Rotational Stiffness of FSA Joint

5.1. Mechanical State of Fan-Shaped Assembled Joint under Out-of-Plane Bending

Figure 12 shows force diagrams for the FSA joint specimen under transverse loading (which induces out-of-plane bending), where L is the length of the member, h is the bolt spacing (taking two bolts as an example), and F is the transverse load.

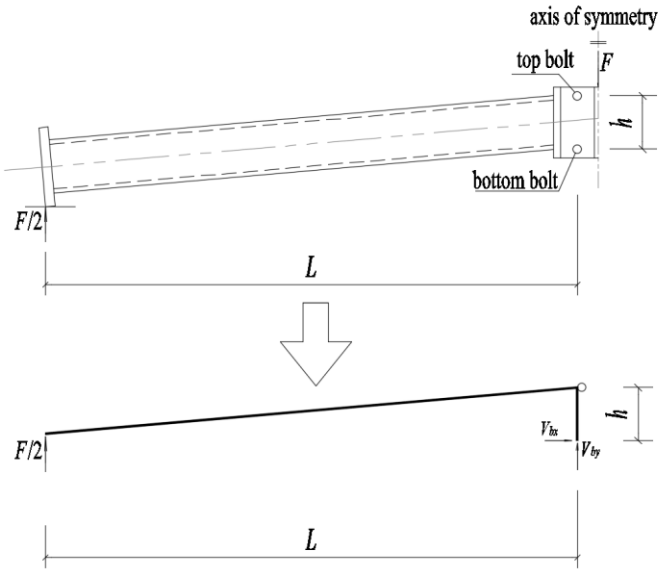


Figure 12. Diagram of joint force under transverse loading.

Based on Figure 12, the shear forces in the X and Y directions and the total shear force on the bottom bolt of the joint under transverse loading, respectively, can be expressed as follows:

$$\begin{aligned} V_{bx} &= \tfrac{F}{2}\tfrac{L}{h} \\ V_{by} &= \tfrac{F}{2} \\ V_b &= \sqrt{V_{bx}^2 + V_{by}^2} = \tfrac{F}{2}\sqrt{1+\left(\tfrac{L}{h}\right)^2} \end{aligned} \tag{1}$$

The member length L is generally much greater than the bolt spacing h; thus, the bolt shear force V_b calculated by Equation (1) will be very large, which makes the bolt area the weakest point in the FSA joint under out-of-plane bending. This also explains the bolt shear failure of specimen J-A. In addition, under excessive shear force, the deformation of the bolt hole wall will also decrease the rotational stiffness of the joint, which induces the rotational stiffness difference between J-A and J-W in Figure 8.

Since the number and spacing of bolts are directly related to the mechanical performance of the joint, these parameters were selected for our parametric analysis. The parameters considered in our parametric analysis are listed in Table 2.

Table 2. Parameters for our parametric analysis of the joints under out-of-plane bending.

Parameters	Values
Bolt spacing/mm	100, 120, 140, 160, 180
Number of bolts	2, 3, 4

5.2. Influence of Bolt Spacing

Five joint models with bolt spacings of 100, 120, 140, 160, 180 mm, respectively, were established by using the finite element software Ansys Version 19.0. The bolt yield strength was 900 MPa. The bolt diameter, the number of bolts, and the thickness of the outer arc plate were 16 mm, 2, 20 mm, respectively. The steel material was Q235B.

Figure 13 shows the bending moment–rotation curves for different bolt spacings. Although the characteristics of each curve are relatively similar, the stiffness and ultimate bearing capacity are obviously different. When the bolt spacing gradually increases from 100 mm to 180 mm, the bending stiffness of the joint also increases gradually. When the rotation angle reaches 0.046 rad, the vertical displacement of the joint reaches 29.6 mm, exceeding 1/50 of the specimen span. The corresponding bending moment is considered as the ultimate bending moment, which, herein, is referred to as M_u (just for comparison).

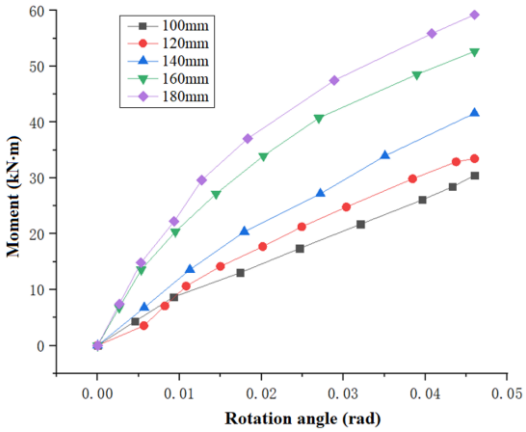


Figure 13. Bending moment–rotation curves of joints with different bolt spacings.

Figure 14 shows the trend of M_u with bolt spacing. With an increase in bolt spacing, the M_u clearly increases. The M_u value at 180 mm spacing is 94% higher than that at 100 mm bolt spacing.

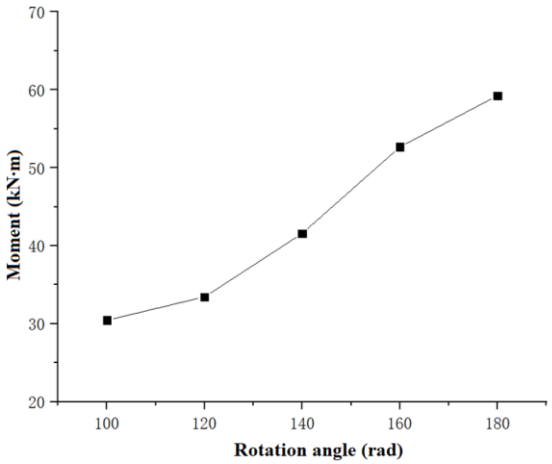


Figure 14. Relationship between joint ultimate bending moment and bolt spacing.

Since increasing the bolt spacing can significantly improve the bending stiffness and ultimate bearing capacity of the joint, it is recommended that the bolt spacing h should be increased as much as possible when the joint detail allows, and h should at least reach the section height of the member.

5.3. Influence of the Number of Bolts

We conducted tests after adjusting the number of bolts to two, three, and four, and the other parameters were as follows: bolt grade 10.9, bolt diameter 16 mm, and steel material Q235. The bending moment–rotation curves with different bolt numbers are shown in Figure 15, and the relationship between the ultimate bending moment and the bolt number is shown in Figure 16.

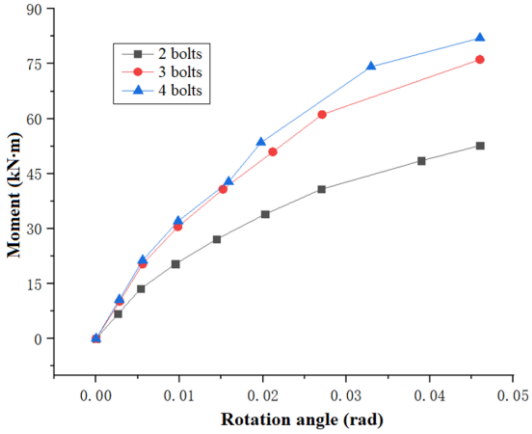


Figure 15. Moment–rotation curves of joints with different amounts of bolts.

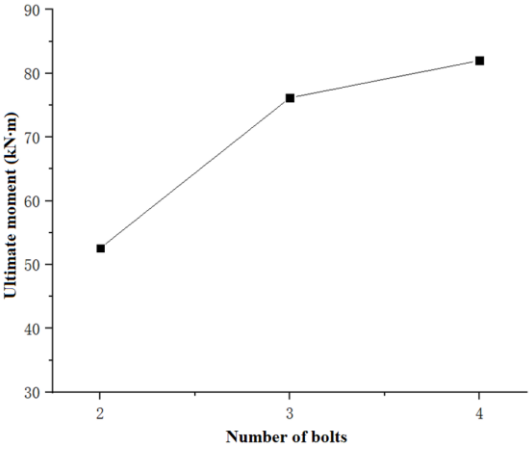


Figure 16. Relationship between the ultimate moment and the number of bolts.

Figure 15 shows that when the number of bolts increases from two to three, the bending stiffness and ultimate moment increase remarkably, but when the number of bolts increases from three to four, the increase amplitude becomes relatively small.

It can be seen from Figure 16 that the ultimate moment of the joint with three bolts is 76.2 kN·m, which is 45.0% higher than that with two bolts. For a joint with four blots, the ultimate moment is 82.0 kN·m, which is only 7.6% higher than that with three bolts, indicating that although increasing the number of bolts can improve the bending capacity of the joint, there is an optimal bolt number. Moreover, too many bolts will increase the construction difficulty. The most appropriate number of bolts should be selected according to the specific joint to meet the structural requirements. Under a joint size close to that of the specimens described in this paper, three bolts for each fan-shaped component are most appropriate.

5.4. Parameter Value Suggestions

From the above parametric analysis, it can be seen that the bending stiffness of the FSA joint in a curved shell structure is greatly affected by the bolt spacing and the number of bolts. Increasing the number of bolts and the spacing of the bolts can significantly improve the bending stiffness and ultimate moment of the joint.

The recommended values of the relevant parameters for this type of joint are as follows:

(1) To ensure the joint has a reasonable size, increasing the bolt spacing can increase the bending stiffness and capacity of the joint. The value of the bolt spacing should

be based on the specific joint and should not be too small. It is suggested that the minimum h is the section height of the rectangular member.

(2) With an increase in the number of bolts, the ultimate bending moment and initial stiffness of the joint are improved. Considering the joint's details and degree of construction difficulty, three bolts are recommended for joints with a size close to that of the specimens described in this paper.

6. Theoretical Analysis of the Rotational Stiffness of the Assembled Joint

6.1. Analysis Model

Suppose that both of the neighboring fan-shaped components are connected by two bolts, as shown in Figure 17. The rotational angle at the member end consists of two angles:

(1) Rotational angle θ_1 caused by bolt hole wall;

(2) Rotational angle θ_2 caused by the deformation of the outer arc plate of the fan-shaped component.

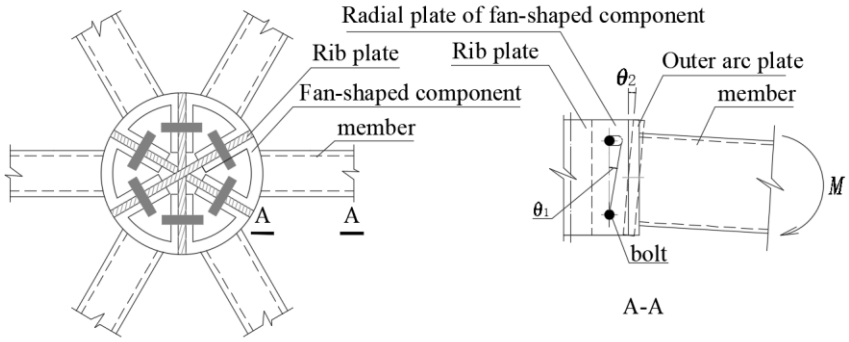


Figure 17. Diagram of joint rotational angle.

The joint rotational stiffnesses corresponding to θ_1 and θ_2 are expressed as follows:

$$k_1 = \frac{\mathrm{d}M}{\mathrm{d}\theta_1}, \quad k_2 = \frac{\mathrm{d}M}{\mathrm{d}\theta_2} \tag{2}$$

Regarding the overall rotational angle, $\mathrm{d}\theta = \mathrm{d}\theta_1 + \mathrm{d}\theta_2 = (1/k_1 + 1/k_2)\mathrm{d}M$; the overall rotational stiffness of the joint is thus computed as follows:

$$k = \frac{\mathrm{d}M}{\mathrm{d}\theta} = \frac{k_1 k_2}{k_1 + k_2} \tag{3}$$

6.2. Derivation of Stiffness k_1

A diagram of rotational angle θ_1 is shown in Figure 18. Both the top and bottom flanges of the member bear axial force under the member end moment M. We assume that the top and flange bear tension and compression force, respectively, with a magnitude of N_1. At the compression area, due to the joint detail feature, the rib plate and the fan-shaped component tend to come closer and closer into contact under the compression force, i.e., the force is transferred by contact. Therefore, the bolt hole wall deformation is not considered at the compression area. At the tension area, conversely, the rib component and fan-shaped component tend to detach from each other under tension force, which causes bolt shear force and bolt hole wall deformation.

Based on the above features, it can be assumed that the rotational center of joint rotation caused by bolt hole wall deformation is located at the bolt center near the bottom flange, and the rotation angle θ_1 is expressed as follows:

$$\theta_1 = \frac{u}{h} \tag{4}$$

where u is the bolt hole wall deformation value, h is the distance between the bolts.

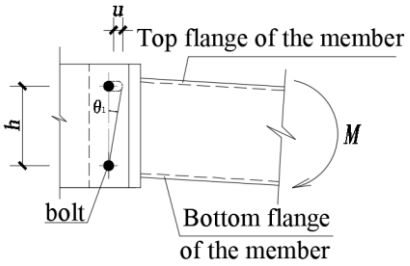


Figure 18. Diagram of rotational angle θ_1.

A diagram for bolt shear force is shown in Figure 19. The bolt hole wall deformation u is determined by bolt shear force V_1, which is related to the angle of fan-shaped component.

$$V_1 = N_1 \cos\left(\frac{\alpha}{2}\right) = \frac{M}{h}\cos\left(\frac{\alpha}{2}\right) \tag{5}$$

where α is the angle between the two radial plates within a fan-shaped component.

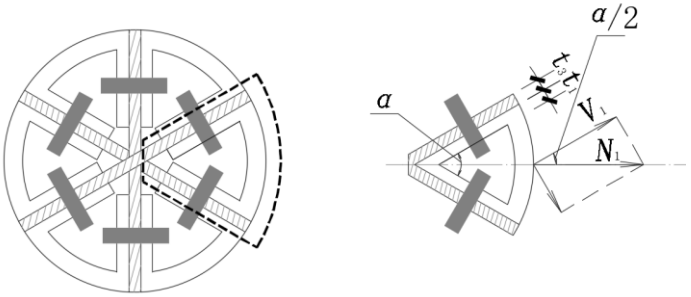


Figure 19. Diagram of bolt shear force V_1.

Referring to [43], the bolt hole wall defamation of the radial plate of the fan-shaped component is as follows:

$$u_{\mathrm{A}} = \frac{1}{4.22}\left(\frac{22}{d}\right)^{\frac{1}{3}}\left(e^{\frac{V_1}{0.0354E\cdot 2t_1}} - 1\right) \tag{6}$$

where t_1 is the thickness of the radial plate of the fan-shaped component, d is the diameter of the bolt (mm), and E is the elasticity modulus of the steel (N/mm^2).

The bolt hole wall defamation of the rib plate is expressed as follows:

$$u_{\mathrm{B}} = \frac{1}{4.22}\left(\frac{22}{d}\right)^{\frac{1}{3}}\left(e^{\frac{V_1}{0.0354E\cdot t_3}} - 1\right) \tag{7}$$

where t_3 is the thickness of the rib plate (mm).

The overall bolt hole wall deformation is calculated as follows:

$$\begin{aligned} u_{\mathrm{AB}} &= u_{\mathrm{A}} + u_{\mathrm{B}} \\ &= \tfrac{1}{4.22}\left(\tfrac{22}{d}\right)^{\frac{1}{3}}\left(e^{\frac{V_1}{0.0354E\cdot 2t_1}} + e^{\frac{V_1}{0.0354E\cdot t_3}} - 2\right) \end{aligned} \tag{8}$$

Considering that the directions of both u_A and u_B are along the direction of V_1, the deformation along the direction of N_1 is as follows:

$$\begin{aligned} u &= u_{\mathrm{AB}}\cos\left(\tfrac{\alpha}{2}\right) \\ &= \tfrac{\cos\left(\frac{\alpha}{2}\right)}{4.22}\left(\tfrac{22}{d}\right)^{\frac{1}{3}}\left(e^{\frac{V_1}{0.0354E\cdot 2t_1}} + e^{\frac{V_1}{0.0354E\cdot t_3}} - 2\right) \end{aligned} \tag{9}$$

From Equations (4)–(9), the rotation angle θ_1 can be expressed as follows:

$$\theta_1 = \frac{\cos\left(\frac{\alpha}{2}\right)}{4.22h}\left(\frac{22}{d}\right)^{\frac{1}{3}}\left(e^{\frac{M\cos(\alpha/2)}{0.0354E\cdot 2t_1\cdot h}} + e^{\frac{M\cos(\alpha/2)}{0.0354E\cdot t_2\cdot h}} - 2\right) \tag{10}$$

From Equations (2) and (10), the rotational stiffness k_1 can be expressed as follows:

$$k_1 = \frac{\mathrm{d}M}{\mathrm{d}\theta_1} = \frac{0.1495Eh^2\left(\frac{d}{22}\right)^{\frac{1}{3}}}{\left(\frac{e^{\frac{M\cos(\alpha/2)}{0.0354E\cdot 2t_1\cdot h}}}{2t_1} + \frac{e^{\frac{M\cos(\alpha/2)}{0.0354E\cdot t_2\cdot h}}}{t_2}\right)\cdot\cos^2\left(\frac{\alpha}{2}\right)} \tag{11}$$

And the initial value of k_1 is as follows:

$$k_{10} = k_1|_{M=0} = \frac{0.1067Eh^2d^{\frac{1}{3}}t_1t_3}{(2t_1+t_3)\cdot\cos^2\left(\frac{\alpha}{2}\right)} \tag{12}$$

6.3. Derivation of Stiffness k_2

The outer arc plate of the fan-shaped component is in an out-of-plane bending state while the member end bending moment is applied to the joint. As shown in Figure 20, the rotation angle θ_2 can be expressed as follows:

$$\theta_2 = \frac{\delta}{\left(\frac{H}{2}\right)} = \frac{2\delta}{H} \tag{13}$$

where δ is the out-of-plane deformation, i.e., the bending displacement of the outer arc plate, and H is the member section height.

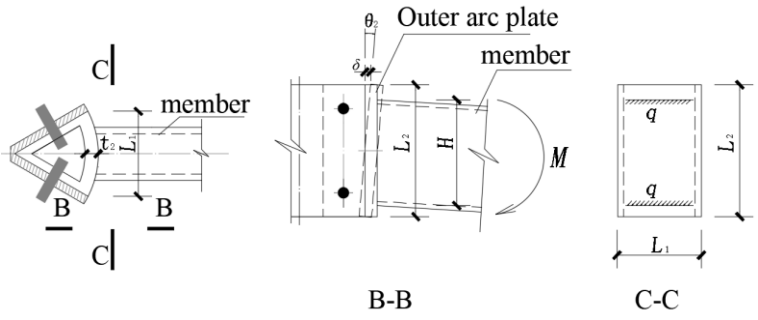


Figure 20. Deformation diagram of outer arc plate.

Suppose that the width, height, and thickness of the outer arc plate are L_1, L_2, and t_2, respectively. The two sides along the direction of L_2 can be considered as the supporting edges of the plate. Two parameters are introduced as follows:

$$\gamma_1 = \frac{L_2}{L_1}, \quad \gamma_2 = \frac{H}{L_2} \tag{14}$$

The axial force N at the top and bottom flanges caused by the member end moment is transformed to line load q along the direction of L_1:

$$q = \frac{N}{L_1} = \frac{M}{HL_1} = \frac{M}{\gamma_2 L_2 L_1} \tag{15}$$

The out-of-plane deformation under q is

$$\delta = \frac{5qL_1^4}{384EI_b} \tag{16}$$

where I_b is the moment of inertia of the plate section within the action range of q:

$$I_b = \frac{bt_2^3}{12} \tag{17}$$

where b is the equivalent height, i.e., the height range affected by q. The true value of the equivalent height is hard to determine. Through numerical examples, it was found that b is mainly related to γ_1 and L_2 as follows:

$$b = 0.45\gamma_1^{-1.25}L_2 \tag{18}$$

Substituting Equations (15), (17), and (18) into Equation (16) yields

$$\delta = \frac{M \cdot \gamma_1^{1.25}L_1^3}{2.88E\gamma_2 t_2^3 L_2^2} \tag{19}$$

Considering $H = \gamma_2 L_2$ and $L_2/L_1 = \gamma_1$, substituting Equation (19) into (13) yields the following:

$$\theta_2 = \frac{M \cdot \gamma_1^{1.25}L_1^3}{1.44E\gamma_2^2 t_2^3 L_2^3} = \frac{M}{1.44E\gamma_1^{1.75}\gamma_2^2 t_2^3} \tag{20}$$

The joint rotational stiffnesses corresponding to θ_2 is as follows:

$$k_2 = \frac{\mathrm{d}M}{\mathrm{d}\theta_2} = 1.44E\gamma_1^{1.75}\gamma_2^2 t_2^3 \tag{21}$$

6.4. Joint Initial Rotational Stiffness and Test Verification

Through substituting Equations (12) and (21) into (3), the overall initial rotational stiffness of the joint can be obtained as follows:

$$\begin{aligned} k_0 &= \frac{k_{10}k_2}{k_{10}+k_2} \\ &= \frac{0.1536Eh^2 d^{\frac{1}{3}} t_1 t_3 t_2^3 \gamma_1^{1.75}\gamma_2^2}{0.1067h^2 d^{\frac{1}{3}} t_1 t_3 + 1.44(2t_1+t_3)t_2^3\gamma_1^{1.75}\gamma_2^2 \cdot \cos^2(\frac{\alpha}{2})} \end{aligned} \tag{22}$$

For specimen J-A, the initial stiffness calculated by Equation (22) is compared with test data in Table 3.

Table 3. Joint initial rotational stiffness comparison.

Method	Joint Initial Rotational Stiffness/kN·m/rad
Calculated by Equation (22)	3.12×10^3
Test	3.36×10^3

The initial stiffness calculated by Equation (22) is slightly smaller than the test result, and the relative error is only 7.14%.

7. Conclusions

Based on our experiments and finite element analysis of a fan-shaped assembled joint for curved lattice shells and corresponding welded joints, the main conclusions of this study are as follows:

(1) The fan-shaped assembled joint shows semi-rigid characteristics, and the specimen experiences three stages: (1) the elastic stage (0–81.5 kN·m), in which the joint shows good bending performance; (2) the elastic–plastic stage (81.5–142.6 kN·m), where the bending stiffness decreases markedly to about half of the initial stiffness, and the rotation increases gradually owing to bolt slippage and deformation of the bolt hole wall; and (3) the plastic failure stage (143–156.5 kN·m), in which the bolt is brittle and the specimen fails, indicating that the key to improving the bending stiffness of the fan-shaped assembled joint is improving the shear strength of the bolt.
(2) The initial rotational stiffness of the FSA joint is about one third of that of the welded joint.
(3) Our parametric analysis shows that the bending stiffness and ultimate moment of the assembled joint increase when the spacing of the bolts and the number of bolts are increased.
(4) The theoretical calculation formula proposed in this paper can approximately simulate the joint initial rotational stiffness of the fan-shaped assembled joint.

The present study has limitations, including the fact that it only considered a small number of FSA joint specimens and limited loading cases. Future experimental and numerical investigations are needed to explore the mechanical behavior of FSA joints subjected to complex loading cases such as bending–compression loads.

Author Contributions: Writing—original draft preparation, J.X.; writing—review and editing, Y.Z.; conceptualization, J.W. and J.L.; formal analysis, Q.Z.; investigation, W.W. All authors have read and agreed to the published version of the manuscript.

Funding: The financial support the authors received from the National Natural Science Foundation of China (NSFC) via Grant No. 52378179.

Data Availability Statement: The raw data supporting the conclusions of this article will be made available by the authors on request.

Conflicts of Interest: Author Jin Lu is employed by the company Hangzhou Yuexiu Real Estate Development Co., Ltd. Author Qian Zhang is employed by the company Shanghai Pudong New Area Construction (Group) Co., Ltd. The remaining authors declare that the research was conducted in the absence of any commercial or financial relationships that could be construed as a potential conflict of interest.

References

1. Ma, H.H.; Ma, Y.Y.; Fan, F.; Zhang, Y.N. Seismic performance of single-layer spherical reticulated shells considering joint stiffness and bearing capacity. *Adv. Steel Constr.* **2022**, *18*, 604–616.
2. Xu, J.S.; Fang, C.; Wang, W.; Chen, G.M. Structural design of irregular curved lattice shells in China. *Proc. Inst. Civ. Eng.-Civ. Eng.* **2019**, *172*, 37–47. [CrossRef]
3. Zhao, Z.W.; Zhu, H.; Chen, Z.H. Mechanical behavior of single-layer reticulated shell connected by welded hollow spherical joints with considering welding residual stress. *Weld. World* **2016**, *60*, 61–69. [CrossRef]
4. Xing, J.H.; Chen, A.G.; Yang, Q.S. In-plane bending hysteretic behavior of cruciform diaphragm welded joints with axial force. *J. Constr. Steel Res.* **2017**, *132*, 164–178. [CrossRef]
5. Wang, X.Y.; Li, H.W.; Song, X.Y. Experimental investigation of failure mechanism of grid structure with bolted spherical joints. *J. Constr. Steel Res.* **2022**, *188*, 107033. [CrossRef]
6. Wu, Q.Y.; Wang, H.J.; Qian, H.L.; Han, K.; Fan, F. Effect of insufficient screwing depth of bolt on mechanical behavior of bolt-ball joint and stability of single-layer reticulated shell. *Eng. Struct.* **2020**, *213*, 110590. [CrossRef]
7. Tian, J.P.; Wang, X.Y.; Li, H.W.; Wang, Z.; Pan, J.R. Ultra-low cycle fatigue performance of grid structure with bolted spherical joints. *J. Constr. Steel Res.* **2023**, *201*, 107728. [CrossRef]
8. Yang, D.B.; Li, M.J.; Fu, F.; Wu, J.Z. Experimental and numerical studies on a new type of bolt-ball joint for spatial grid structures. *J. Constr. Steel Res.* **2022**, *188*, 107035. [CrossRef]
9. Du, B.; Yan, Y.J.; Yan, B. Finite element analysis of the hollow spherical shells plus bolts joints used for grid structures under uniaxial compression. *IOP Conf. Ser. Earth Environ. Sci.* **2020**, *567*, 012009. [CrossRef]
10. Gidófalvy, K.; Katula, L.; Ma, H.H. Free-form grid shell structures on rectangular plan with semi-rigid socket joints. *J. Int. Assoc. Shell Spat. Struct.* **2016**, *57*, 295–306. [CrossRef]
11. Ma, H.H.; Ma, Y.Y.; Yu, Z.W.; Fan, F. Experimental and numerical research on gear-bolt joint for free-form grid spatial structures. *Eng. Struct.* **2017**, *148*, 522–540. [CrossRef]

12. Ma, Y.Y.; Ma, H.H.; Yu, Z.W.; Fan, F. Experimental and numerical study on the cyclic performance of the gear-bolt semi-rigid joint under uniaxial bending for free-form lattice shells. *J. Constr. Steel Res.* **2018**, *149*, 257–268. [CrossRef]
13. Ma, H.H.; Wang, W.; Zhang, Z.H.; Fan, F. Research on the static and hysteretic behavior of a new semi-rigid joint (BCP joint) for single-layer reticulated structures. *J. Int. Assoc. Shell Spat. Struct.* **2017**, *58*, 159–172. [CrossRef]
14. Guo, X.N.; Huang, Z.W.; Xiong, Z.; Yang, S.F.; Peng, L. Experimental studies on behaviour of bolted ball-cylinder joints under axial force. *Steel Compos. Struct.* **2016**, *21*, 137–156. [CrossRef]
15. Jin, Y.D.; Wang, R.H.; Zhao, Y. Experiment of six-member basic structure with a pre-embedded-bolt joint for single-layer latticed shells. *J. Zhejiang Univ. (Eng. Sci.)* **2020**, *54*, 2100–2108. (In Chinese)
16. Mahyar, M.; Suleyman, N.O.; Merve, S.; Burak, K.C. Analyzing of bolted joints for connecting rectangular hollow sections in reticulated shells. *Archit. Eng. Des. Manag.* **2023**, *19*, 550–566.
17. Zhang, A.L.; Li, C.; Zhang, Y.X.; Liu, X.C. Static test and theoretical study on semirigid pin joint for modular steel reticulated shell. *Struct. Des. Tall Spec. Build.* **2022**, *31*, e1932. [CrossRef]
18. Zhang, A.L.; Li, C.; Zhang, Y.X.; Liu, X.C. Experimental and theoretical analyses on semi-rigid pin joints under in-plane direction bending in modular reticulated shell. *J. Constr. Steel Res.* **2022**, *190*, 101128. [CrossRef]
19. Mashrah, W.A.H.; Chen, Z.H.; Liu, H.B.; Amer, M.A. Static performance of novel steel dovetail joints for single-layer grid shells under out-of-plane bending moments. *J. Constr. Steel Res.* **2021**, *187*, 106988. [CrossRef]
20. Mashrah, W.A.H.; Chen, Z.H.; Liu, H.B.; Amer, M.A. Mechanical behaviour of a novel steel dovetail joint subjected to axial compression loading. *Eng. Struct.* **2021**, *245*, 112852. [CrossRef]
21. Mashrah, W.A.H.; Chen, Z.H.; Liu, H.B. Numerical and Theoretical Study on Mechanical Behaviors of New Dovetail Joint System (NDJs) Subjected to Tensile, Compressive, and Out-of-plane Bending Moment Forces. *Int. J. Steel Struct.* **2021**, *21*, 1108–1133. [CrossRef]
22. Mashrah, W.; Chen, Z.H.; Boufendassa, R.; Liu, H.B. Numerical Parametric Study on Hysteresis Performance of the Novel Dovetail Joint for Single-layer Grid Shells Subjected to Out-of-Plane Bending Moment. *KSCE J. Civ. Eng.* **2023**, *27*, 3952–3970. [CrossRef]
23. Xu, Y.; Zhang, X.N.; Han, Q.H. Research on the progressive collapse resistance of single-layer cylindrical latticed shells with AH joints. *Thin-Walled Struct.* **2021**, *158*, 107178. [CrossRef]
24. Han, Q.H.; Wang, C.X.; Xu, Y.; Zhang, X.N.; Liu, Y.M. Mechanical performance of AH joints and influence on the stability behaviour of single-layer cylindrical shells. *Thin-Walled Struct.* **2020**, *146*, 106459. [CrossRef]
25. Han, Q.H.; Liu, Y.M.; Xu, Y.; Li, Z.Y. Mechanical behaviours of assembled hub joints subjected to axial loads. *J. Construct. Steel Res.* **2019**, *153*, 667–685. [CrossRef]
26. Yang, D.B.; Fan, K.; Zhou, G.G.; Wang, H.; Yang, H.; Zhang, M.; Zhu, B.C. Study on the mechanical performances of single-layer latticed domes with SLO joints based on beam elements FE model. *J. Build. Eng.* **2023**, *76*, 107284. [CrossRef]
27. Zhang, A.L.; Liu, T.Y.; Zhang, Y.X.; Liu, X.C.; Jiang, Z.Q. Experimental and numerical research on mechanical behavior of prestressed high-strength bolt joint. *J. Constr. Steel Res.* **2021**, *182*, 106690. [CrossRef]
28. Ma, H.H.; Issa, A.M.; Fan, F.; Zhang, Z.H.; Adeoti, G.O. Numerical study and design method of a single-layer spherical reticulated dome with hollow ball-tube bolted joints. *J. Int. Assoc. Shell Spat. Struct.* **2017**, *58*, 137–144. [CrossRef]
29. Feng, R.Q.; Liu, F.C.; Yan, G.R.; Chang, X.L. Mechanical behavior of Ring-sleeve joints of single-layer reticulated shells. *J. Constr. Steel Res.* **2017**, *128*, 601–610. [CrossRef]
30. Feng, R.Q.; Liu, S.; Dai, C.L. Performance of freeform single-layer assembled reticulated shells with double-ring joints. *Eng. Struct.* **2021**, *232*, 111802. [CrossRef]
31. Zhang, Z.J.; Feng, R.Q.; Cai, Q.; Yan, G.R. Experimental and simulation study on the hysteretic behavior of double-ring joints for a single-layer grid shell under cyclic eccentric loading. *J. Constr. Steel Res.* **2022**, *195*, 107346.
32. Zheng, L.; Qu, X.R.; Guo, H.; Geng, S.B. Experimental Study on a New Connection Method of Latticed Shell Joint. *KSCE J. Civ. Eng.* **2021**, *25*, 3409–3423. [CrossRef]
33. Zheng, L.; Qin, C.; Guo, H.; Zhang, D.P.; Zhou, M.T.; Geng, S.B. Experimental and finite element study on the single-layer reticulated composite joints. *Adv. Struct. Eng.* **2020**, *23*, 2174–2187. [CrossRef]
34. Liu, J.Y.; Lee, Y.C.; Cardoso Llach, D. Computational design and fabrication of highly customizable architectural space frames: Making a flat-cut Weaire-Phelan structure. *Int. J. Archit. Comput.* **2021**, *19*, 37–49. [CrossRef]
35. Rossot, D.; Machado, R.D.; Barbieri, N.; de Lima, K.F. Experimental and numerical study of a geodesic dome under static and dynamic loads and the influence of nodal connections. *Exp. Tech.* **2022**, *46*, 823–834. [CrossRef]
36. Mashrah, W.A.H.; Chen, Z.H.; Liu, H.B.; Rima, B.; Mogalli, A. Static performance of steel temcor joint subjected to out-of-plane bending moments. *Structures* **2022**, *39*, 882–900. [CrossRef]
37. Mashrah, W.A.H.; Chen, Z.H.; Liu, H.B.; Rima, B.; Mogalli, A. Static performance of steel temcor joints subjected to axial tension and compression loads. *Structures* **2023**, *47*, 1113–1133. [CrossRef]
38. Wu, J.Z.; Li, Y.H.; Sun, G.J.; Chen, S. Experimental and numerical analyses of the hysteretic performance of an arched aluminium alloy gusset joint. *Thin-Walled Struct.* **2022**, *171*, 108765. [CrossRef]
39. Ge, H.B.; Wan, H.P.; Shen, Y.B.; Yang, C.; Luo, Y.Z. Rotational performance of semi-rigid plate-type joints for reticulated shell structures composed of plate members. *Eng. Struct.* **2023**, *283*, 115815. [CrossRef]

40. Miao, F.; Dong, S.L.; Liang, H.Q.; Wang, X.T.; Zhu, X.L.; Ding, C. Manufacture and prefabrication practice on a test model of a novel six-bar tetrahedral cylindrical lattice shell. *Adv. Struct. Eng.* **2019**, *22*, 287–296. [CrossRef]
41. Tan, Y.L.K.; Zhang, Y.; Zhang, Q.W.; Fan, F. Structural performance of a novel combined nested bolted joint for aluminum alloy mega-latticed structures. *Structures* **2023**, *57*, 105246. [CrossRef]
42. *GB/T 228.1-2010*; Metallic Materials-Tensile Testing-Part 1: Method of Test at Room Temperature. General Administration of Quality Supervision, Inspection and Quarantine of the People's Republic of China: Beijing, China, 2010. (In Chinese)
43. Xu, J.S.; Chen, Y.Y.; Han, L.; Deng, C.G. Slip process analysis of regular bolt and bearing type high-tensile bolt shear connections. *J. Tongji Univ.* **2003**, *31*, 510–514.

Disclaimer/Publisher's Note: The statements, opinions and data contained in all publications are solely those of the individual author(s) and contributor(s) and not of MDPI and/or the editor(s). MDPI and/or the editor(s) disclaim responsibility for any injury to people or property resulting from any ideas, methods, instructions or products referred to in the content.